

# Single magnetic adsorbates on $s$ -wave superconductors

Benjamin W. Heinrich,<sup>1,\*</sup> Jose I. Pascual,<sup>2,3,†</sup> and Katharina J. Franke<sup>1,‡</sup>

<sup>1</sup>*Fachbereich Physik, Freie Universität Berlin, 14195 Berlin, Germany*

<sup>2</sup>*CIC nanoGUNE, 20018 Donostia-San Sebastián, Spain*

<sup>3</sup>*Ikerbasque, Basque Foundation for Science, 48011 Bilbao, Spain*

(Dated: November 3, 2017)

In superconductors, magnetic impurities induce a pair-breaking potential for Cooper pairs, which locally affects the Bogoliubov quasiparticles and gives rise to Yu-Shiba-Rusinov (YSR or Shiba, in short) bound states in the density of states (DoS). These states carry information on the magnetic coupling strength of the impurity with the superconductor, which determines the many-body ground state properties of the system. Recently, the interest in Shiba physics was boosted by the prediction of topological superconductivity and Majorana modes in magnetically coupled chains and arrays of Shiba impurities.

Here, we review the physical insights obtained by scanning tunneling microscopy into single magnetic adsorbates on the  $s$ -wave superconductor lead (Pb). We explore the tunneling processes into Shiba states, show how magnetic anisotropy affects the phase diagram, and determine the crossing of the many-body groundstate through a quantum phase transition. Finally, we discuss the coupling of impurities into dimers and chains and their relation to Majorana physics.

## CONTENTS

I. Introduction	1
II. Yu-Shiba-Rusinov bound states in $S$ -wave superconductors	2
A. Magnetic impurities on a superconductor	2
B. Resolving Yu-Shiba-Rusinov states in tunneling spectroscopy	3
III. From single-particle transport to Andreev reflections	5
IV. Orbital character of Yu-Shiba-Rusinov states	7
V. Quantum-phase transition from a Kondo-correlated to a superconducting ground state	8
A. Multiple magnetic ground states in a magnetic molecular system	9
B. Interplay of Kondo correlations with Yu-Shiba-Rusinov excitations	10
C. Effect of magnetic anisotropy in Yu-Shiba-Rusinov states	10
VI. Lateral extension of Yu-Shiba-Rusinov states	12
VII. Coupling of Shiba impurities – from dimers to topological chains	13
VIII. Conclusions and future directions	14
Acknowledgments	14
References	14
References	14

## I. INTRODUCTION

Over the last decade, the interest in low-dimensional hybrid superconductor-magnet systems increased dramatically. It was realized that these condensed matter systems are prime candidates to bear topological phases and, in particular, Majorana zero modes [1–3]. As a consequence, this triggered a renewed interest in the long-standing problem of magnetic impurities in superconductors and led to numerous theoretical publications in recent years [4–27].

Experimentally, the investigation of single impurities and their influence on the local environment became possible with the technological advances in scanning probe techniques over the last decades. These developments enable the *in vacuo* preparation of clean superconductor surfaces, the deposition of single atoms at low temperatures, and their investigation with high spatial and energetic resolution at temperatures well below the critical temperature of the superconductor  $T_c$ . After the pioneering work from the Don Eigler group in 1997 [28] on single Manganese (Mn) and Gadolinium (Gd) adatoms on a Niobium (Nb) single crystal surface at 4 K, it took more than ten years until new experiments with increased energy resolution were published [29, 30]. Experiments at lower temperatures and the use of superconducting tips enabled a more detailed analysis of Yu-Shiba-Rusinov (YSR) [31–34] bound states induced by single paramagnetic adsorbates on the  $s$ -wave superconductor Pb. In this overview article, we review the experimental progress made in this field since then.

In Section II, we will start with a short introduction to the physical concepts of YSR states but refrain from a detailed theoretical treatment, which can be found, *e.g.*, in the review by Balatsky and coworkers [6]. We then will discuss the experimental detection mechanism

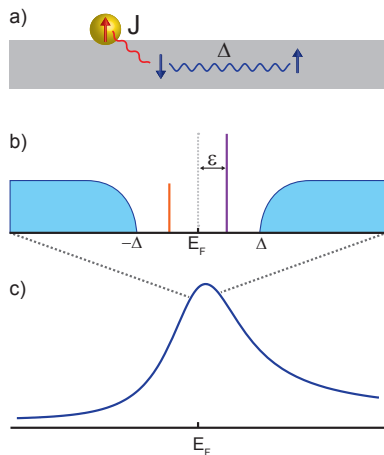


Figure 1. a) A paramagnetic impurity in contact with an  $s$ -wave superconductor. The electron-phonon coupling provides a positive interaction  $\Delta$  between electrons of opposite spin and momentum and couples these into Cooper pairs. The impurity spin is exchange coupled with strength  $J$  to the Cooper pairs. It locally breaks time-reversal symmetry and, therefore, possesses a pair-breaking potential. b) This interaction induces pairs of bound states symmetric to  $E_F$  within the gap of the quasiparticle excitation spectrum. For strong coupling ( $k_B T_K \gtrsim \Delta$ ) additionally a Kondo resonance occurs outside the excitation gap.

of YSR states in tunneling experiments and their relation to Andreev bound states as observed in superconducting quantum dot experiments. In Sec. III, the transport processes through subgap states are studied, while in Sec. IV we review the orbital nature of these states. In Sec. V, we explore the effect of magnetocrystalline anisotropy on the many-body phase diagram and determine the ground state's spin, which undergoes a quantum phase transition caused by a varying exchange coupling strength. In Sec. VI we detail the origin of extended wave functions of the bound states. Finally, in Sec. VII, we explore the hybridization of single impurities and will end the review with an outlook on future research directions in Sec. VIII.

## II. YU-SHIBA-RUSINOV BOUND STATES IN $S$ -WAVE SUPERCONDUCTORS

A magnetic impurity on a metallic surface in the normal state bears a scattering potential for substrate electrons. It consists of an exchange term  $JS$  with  $J$  being the exchange coupling strength of the spin state  $S$  of the impurity with the substrate and of a potential scattering term  $U$ . The scattering gives rise to screening of the charge and spin, which depends on the DoS around the Fermi level. Lowering the temperature below the temperature of the superconducting phase transition opens up an excitation gap around the Fermi level ( $E_F$ ). This affects the scattering at the magnetic impurity.

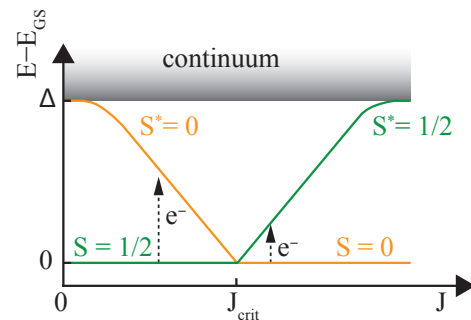


Figure 2. Quasiparticle excitation diagram for a classical spin  $1/2$  impurity on a superconductor. The exchange coupling  $J$  with a local spin induces a low-lying state into the excitation gap of the superconductor. With increasing exchange coupling  $J$ , a quantum phase transition changes the parity of the ground state from  $S = 1/2$  to  $S = 0$ , with  $S$  being the manybody spin of the total system.

The localized spin in an  $s$ -wave superconductor breaks time-reversal symmetry. It exchange scatters with the superconductor's quasiparticles and, hence, possesses a pair-breaking potential [35]. Locally, this yields a suppression of the gap and a pair of intragap bound states. In the limit of high impurity densities, the scattering results in a breakdown of superconductivity.

### A. Magnetic impurities on a superconductor

Figure 1a presents a sketch of the important energy scales of the single-impurity problem: the exchange coupling  $J$  with the condensate competes with the superconducting pairing energy  $\Delta$ . The interaction of the local spin with the Cooper pairs then gives rise to a low-lying excited state within the gap of the quasiparticle excitation spectrum as was deduced independently by Luh Yu [31], Hiroyuki Shiba [32], and A. I. Rusinov [33, 34] for a classical spin. Computationally, this can be realized by setting  $J \rightarrow 0$ , the impurity spin  $S \rightarrow \infty$ , and  $JS = \text{finite}$ . The induced YSR bound state, which is, for the sake of convenience, often just called Shiba state, is a low-lying excitation of the many-body state within the excitation gap of the superconductor (Fig. 2). Its energy has been derived from a Bogoliubov transformation of the Hamiltonian of the combined impurity-BCS-superconductor system [31, 33], or via a Green's function formulation, where the single-impurity problem is solved via the T matrix [32, 34]. The bound state possesses an energy:

$$\varepsilon = \Delta \frac{1 - a^2}{1 + a^2}, \quad (1)$$

where  $a = JS\pi\rho_s$ , with  $\rho_s$  being the DoS at  $E_F$  in the normal state.

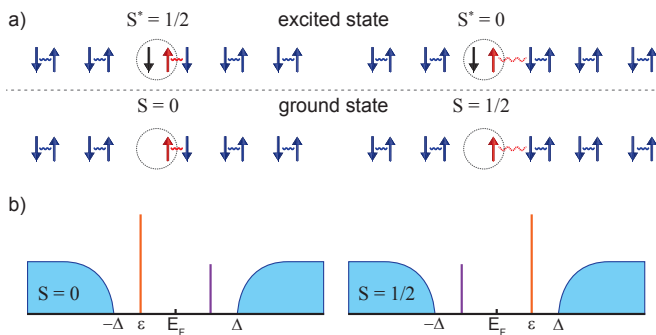


Figure 3. a) Sketch of the two coupling regimes of a spin 1/2 impurity on an  $s$ -wave superconductor: in the Kondo-screened case ( $k_B T_K \gtrsim \Delta$ ), the coherent many-body ground state has zero net spin ( $S = 0$ ). The attachment of a tunneling electron then increases the spin to 1/2 in the excited state ( $S^* = 1/2$ ). In the free-spin case ( $k_B T_K \lesssim \Delta$ ), the screening of the local spin is incomplete and the many-body ground state spin is  $S = 1/2$ . Here, the attachment of a tunneling electron induces the transition into an excited state with  $S^* = 0$ . b) The transition from one to the other ground state by, *e.g.*, changing  $J$ , is accompanied by an inversion of the relative spectral weight of the electron and hole-like components of the bound state pair.

In the case of a quantum spin, the exchange coupling to the quasi-particle reservoir gives rise to Kondo screening as known for spins in normal metals [36]. The formation of the Kondo singlet state then competes with the superconducting ground state [37]. For strong coupling, *i.e.*,  $k_B T_K \gg \Delta$ , a correlated Kondo state is formed, which screens the impurity spin and reduces the total spin to zero. Here,  $k_B$  is the Boltzmann constant and  $T_K$  the Kondo temperature. In tunneling spectroscopy, a Kondo resonance is detected with a width of approximately  $k_B T_K$  (Fig. 1c), while the bound states merge with the gap edge. In the case of vanishing coupling, *i.e.*,  $k_B T_K \ll \Delta$ , no screening occurs because the opening of the superconducting gap depletes the DoS on the Kondo energy scale  $k_B T_K$  around  $E_F$ . Again the bound states lie exponentially close to the gap edge. In this case, the total spin of the system is  $S > 0$ . [38] The problem of a quantum mechanical spin was first solved by Matsuura [37]. The energy of the YSR state depends on the Kondo temperature  $T_K$  and can be calculated, in the limit of  $k_B T_K \gg \Delta$ , using Eq. 1 and

$$a \approx \frac{\pi \Delta}{4 k_B T_K} \ln \frac{4 k_B T_K}{\pi \Delta} e. \quad (2)$$

An interesting situation arises, when both involved energy scales are similar:  $k_B T_K \sim \Delta$ . Then, the YSR excitations lie well within the excitation gap of the superconductor (Fig. 3b) and correspond to excitations that change the spin of the many-body system by  $\Delta S = \pm 1/2$ . A first order quantum phase transition between the free-spin situation for weak coupling and the Kondo-screened

situation for strong coupling occurs at  $k_B T_K \approx 0.3 \Delta$  as calculated by numerical renormalization group theory [39, 40] (Fig. 2). This level crossing of the two lowest states, a singlet and a doublet, has been treated in depth theoretically [6, 8, 37, 39–43]. It is accompanied by a crossing of the particle- ( $u$ ) and hole-like ( $v$ ) components of the bound state and a characteristic change of their weight [39, 40] as illustrated in Fig. 3b. The spectral weight of  $u$  and  $v$  is influenced by the Coulomb potential [6], which breaks particle-hole symmetry, and by asymmetries in the normal state conductance of the superconductor [44, 45].

In the simplest case of a spin 1/2 impurity, a YSR bound state in the excitation spectra corresponds to a quasiparticle excitation from the ground state, either singlet or doublet, to a first excited state, a doublet or singlet state, respectively, which exists within the gap of the excitation spectrum (Fig. 3a). All other excitations of the system lie within the continuum of excitations outside the gap. In general, this first excitation changes the total spin by  $\Delta S = \pm 1/2$  and transfers the system from the free-spin to the Kondo-screened state or vice versa. For an infinite system, it is irrelevant whether this excitation occurs via the hole- or the particle-like component of the state, *i.e.*, via adding or extracting an electron from the system [6].

Now, we want to consider the spatial extend of the wave function  $\psi$  of the YSR state. The excitations of  $u$  and  $v$  are symmetric in energy to  $E_F$  in the quasiparticle excitation spectrum [Fig. 1(b)] [46]. In the case of a point-like scatterer in a three-dimensional (3D) superconductor with an isotropic Fermi surface, their wave function  $\psi^+$  and  $\psi^-$ , respectively, scale with  $r$  like follows:

$$\psi^\pm(r) \propto \frac{\sin(k_F r + \delta^\pm)}{k_F r} \exp\left[-|\sin(\delta^+ - \delta^-)| \frac{r}{\xi}\right]. \quad (3)$$

Both,  $\psi^+$  and  $\psi^-$  oscillate with  $k_F r$  (the Fermi wave vector times the distance from the impurity), but show a different scattering phase shift  $\delta^\pm$ . Interestingly, the energy of the bound state is related to the difference in the scattering phase shift for  $u$  and  $v$ :

$$\epsilon = \Delta \cos(\delta^+ - \delta^-). \quad (4)$$

The wave functions' fall-off away from the impurity is dominated by the factor  $1/(k_F r)$  for short distances. But for large distances, the exponential decay dominates, which depends on the superconducting coherence length  $\xi$ .

## B. Resolving Yu-Shiba-Rusinov states in tunneling spectroscopy

In a tunnel junction, the above mentioned excitation is induced by particles (holes) tunneling between the two

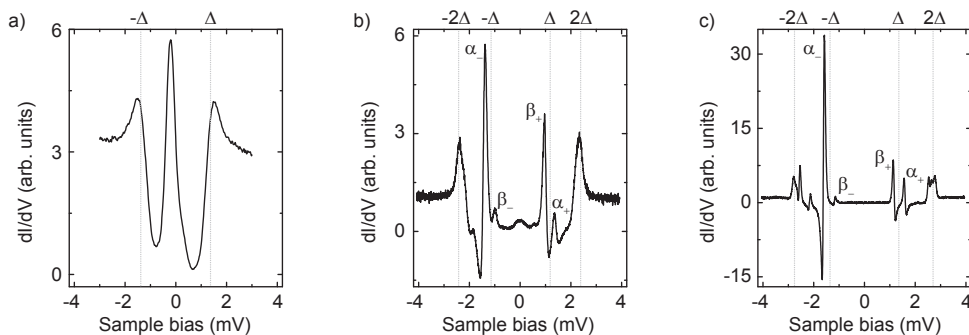


Figure 4. Tunneling spectra of Mn adatoms on Pb(111) acquired with a metal tip at 1.2 K (a), or with a superconducting Pb-covered tip at 4.8 K (b), and 1.2 K (c), respectively. Different numbers of YSR resonances are resolved depending on the tip material and the temperature. Figure adapted from Ref. [47].

electrodes via the bound state. Hence,  $u$  and  $v$  are probed in spectra of the differential conductance  $dI/dV$  as resonances at opposite bias with respect to  $E_F$  within the superconducting gap. As a typical example, Fig. 4 shows a  $dI/dV$  spectrum of a Mn adatom on Pb(111).

If a metallic tip is used as second electrode (spectrum in Fig. 4a), tunneling into the electron and hole component of the bound state sets in at a sample bias of  $eV = \pm\epsilon$  as sketched in Fig. 5a. Tunneling into the excitation continuum occurs only for  $|eV| \geq \Delta_{\text{sample}}$ . The energy resolution (usually) is limited by the temperature-dependent Fermi-Dirac broadening of the Fermi edge of the tip ( $\approx 300 \mu\text{V}$  at 1.2 K), which yields sizeable smearing of the YSR resonances. To illustrate this broadening, we show in Figure 4a a  $dI/dV$  spectrum recorded on a Mn atom on Pb(111). We resolve only a single YSR resonance at negative bias. At positive bias, a shoulder appears, which is linked to the electron component  $u$  of the YSR state, but cannot be resolved unambiguously.

In order to circumvent the thermal limit of the energy resolution, superconducting tips were used by several groups [29, 30, 48–51]. These tips probe the sample DoS with the sharp features of the BCS-like tip DoS instead of a temperature-broadened Fermi edge of a metal tip (see Fig. 5b). This yields a considerable gain in energy resolution already at 4.8 K (Fig. 4b). Yet, the spectrum is a convolution of the sharp features in the tip and sample DoS: the spectral function of the sample is probed by the electron and hole quasiparticle resonances at  $+\Delta_{\text{tip}}$  and  $-\Delta_{\text{tip}}$ , respectively ( $\Delta_{\text{tip}}$  is the energy of the gap parameter of the tip). Hence, the spectral function of the sample appears shifted by  $\pm\Delta_{\text{tip}}$ . A subgap resonance with energy  $\epsilon$  (e.g.,  $\alpha_{\pm}$  in Fig. 4b) appears at  $eV = \pm(\Delta_{\text{tip}} + \epsilon)$ , i.e., when the electron-like singularity in the tip's spectral function is aligned with the hole component of the Shiba excitation and vice versa (see Fig. 5b for a sketch of the tunneling configuration).

Additionally, thermally activated tunneling [47, 49, 52, 53] occurs at  $eV = \pm(\Delta_{\text{tip}} - \epsilon)$ , i.e., when the opposite component of the YSR excitation is aligned with the sin-

gularity in the tip spectral function (Fig. 5c). This gives rise to resonances  $\beta_{\pm}$  in Fig. 4b, because tunneling is enabled by a thermal population of  $u$  and  $v$ , respectively.

In order to extract the actual spectral function of the sample, a deconvolution of the  $dI/dV$  spectra is possible. However, this requires knowledge of the tip spectral function, which can usually be inferred from spectra of the pristine superconductor. Then, either a direct deconvolution [54], or a fit of convoluted spectral functions to the  $dI/dV$  [52] can be performed.

A further increase in energy resolution is achieved by lowering the experimental temperature. The  $dI/dV$  spectrum in Figure 4c was acquired with a superconducting tip at 1.2 K. The spectrum resolves particle and hole excitations of three YSR states. The line width is reduced compared to the spectrum acquired at 4.8 K. The energy resolution can be as good as  $\delta E \approx 50 \mu\text{eV}$  at 1.1 K [51]. Interestingly, thermal resonances are only observed for the YSR excitation closest to  $E_F$  ( $\beta_{\pm}$ ). The probability of a thermal excitation of a YSR state (and, hence, the intensity of the thermal resonance in  $dI/dV$ ) depends on the ratio of the excitation energy  $\epsilon$  and the thermal energy  $k_B T$ . The larger  $\epsilon$ , i.e., the further the YSR state is away from  $E_F$ , the smaller is its thermal population (comp. Fig. 5c and 5d). While at 4.8 K all YSR resonances possess thermal counterparts, at 1.2 K, this is limited to excitations close to  $E_F$ . It is noteworthy that at 4.8 K, there is also a sizeable amount of thermal quasiparticles in the pristine superconductor (sample and tip).

Historically, the investigation of single impurities became possible when ultra-high vacuum (UHV) preparation techniques were combined with low temperatures. In 1997, A. Yazdani and co-workers could, for the first time, access YSR states induced by single paramagnetic impurities with an UHV STM operating at 3.8 K [28] (Figure 6a). Furthermore, the lateral resolution of the microscope enabled the detection of the wave function fall-off of the YSR state, which happens on atomic distances on 3D superconductors. These experiments provided the first magnetic fingerprint on a single atom re-

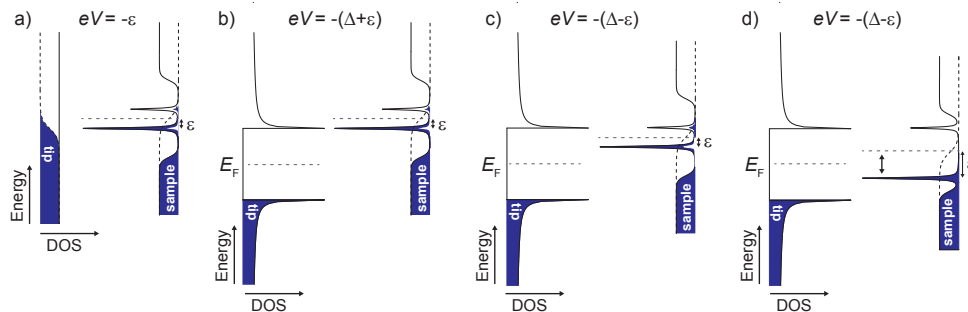


Figure 5. Scheme of the tunneling between a YSR resonance in the sample and the tip DoS with a metallic (a) and a superconducting tip (b – d). a) Tunneling between the occupied component of the YSR state and the tip sets in at a sample bias of  $eV = \pm\epsilon$ . The energy resolution is limited by the thermal broadening of the tip’s Fermi edge. b) At  $eV = -(\Delta_{\text{tip}} + \epsilon)$ , tunneling occurs between the occupied component of the YSR state and the unoccupied BCS-like quasiparticle resonance of the tip. c) At finite temperature, thermally activated tunneling can also occur at  $eV = -(\Delta_{\text{tip}} - \epsilon)$  if the bound state energy  $\epsilon \lesssim k_B T$ . d) If  $\epsilon \gtrsim k_B T$ , no thermal tunneling is observed. Figure adapted from Ref. [52].

solved by low temperature STM, just before the first evidence of Kondo resonances in 1998 [55, 56], and prior to the detection of inelastic excitations of spin eigenstates in 2004 [57], or of a spin-polarized conduction signal in 2007 [58].

Ten years later and with improved energy resolution, multiple Shiba resonances of single Mn and Chromium (Cr) adatoms on Pb films could be resolved using a superconducting Nb tip and lowering the temperature to 0.4 K by Ji *et al.* [29] (Figure 6b). Since then, the field has progressed rapidly. Several groups have focused on resolving the quantum many-body ground state [49, 52], peculiarities in the spatial decay of the YSR wavefunctions [53, 54, 59], the interaction of impurities [60], or different transport processes through the YSR states [47, 61]. In all these investigations, the substrate are *s*-wave superconductors. We will concentrate on these in this review.

However, we need to mention that even prior to these works, several important results were obtained on sub-gap resonances in  $\text{Bi}_2\text{Sr}_2\text{CaCu}_2\text{O}_{8+\delta}$ , a high- $T_c$  cuprate superconductors [62–65]. Yazdani and coworkers [63] showed that intrinsic defects as well as non-magnetic surface adsorbats induce subgap bound states in the excitation gap of this *d*-wave superconductor. Hudson *et al.* finally compared the effect of nominally non-magnetic Zn dopands with paramagnetic Ni impurities [65]. In contrast to *s*-wave superconductors, in a *d*-wave substrate, also these nonmagnetic impurities possess a pair-breaking potential. A more detailed summary of these results can be found in the review of Balatsky, Vekhter, and Zhu [6] and is beyond the scope of this review.

### III. FROM SINGLE-PARTICLE TRANSPORT TO ANDREEV REFLECTIONS

As described in the previous section, excitations of the electron and hole component  $u$  and  $v$  of a YSR bound

state appear as resonances symmetric to  $E_F$  in tunneling spectra of the differential conductance  $dI/dV$ . Single-particle tunneling into/ out off these subgap states excites the impurity–superconductor system from its many-body ground state to the first excited state, which is of a different parity. It is important to note that a continuous single particle current requires an efficient relaxation mechanism of the excitation (*e.g.*,  $\Gamma_1$  in Fig. 7c), with a rate faster than the tunneling rate. An intriguing transport mechanism that comes into play when using superconducting electrodes is the tunneling of electrons through the barrier and its concomitant retroreflection as a hole. This so-called Andreev reflection transfers a Cooper pair from one electrode to the other. Usually,

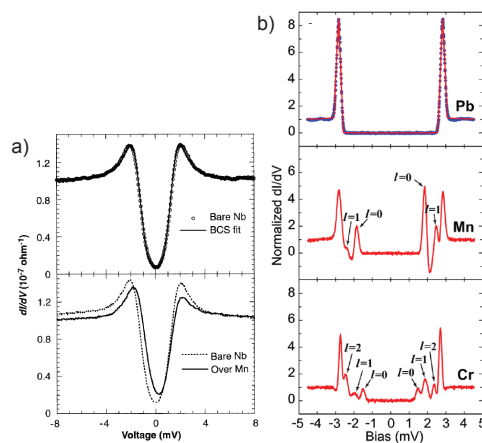


Figure 6. a)  $dI/dV$  spectra over superconducting Nb(110) and over a Mn adatom on Nb measured at 3.85 K with a metallic tip. From Ref. [28]. Reprint with permission from AAAS. b) Mn and Cr adatoms on Pb films present multiple Shiba resonances in the gap.  $dI/dV$  measured with a superconducting Nb tip at 0.4 K. Reprinted figure with permission from Ref. [29]. Copyright 2008 by the American Physical Society.

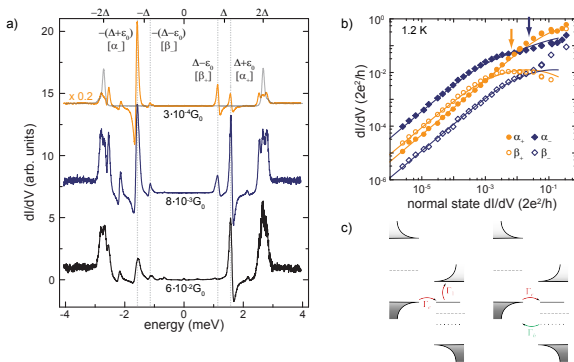


Figure 7. Mn adatom on Pb(111). a)  $dI/dV$  spectra over the adatom at different tip-sample distances acquired at 1.2 K. The relative weight of  $+\alpha$  and  $-\alpha$  in the  $dI/dV$  spectra above the adatom change with the junction resistance. b) Intensity of  $\pm\alpha$  and  $\pm\beta$  as a function of junction resistance. The arrows indicate the turnover from single-particle dominated transport to Andreev dominated transport. c) Sketches of the transport processes through an isolated level in the excitation gap. Single particle transport (left) requires a relaxation to the continuum, while an Andreev reflection transfers a Cooper pair but does not change the occupation of the level. Figure adapted from Ref. [47].

Andreev processes between the quasiparticle continua of tip and sample are only important at strong tunneling coupling [48]. This is easily understood considering that the tunneling barrier has to be overcome twice, by an electron and by its reflected hole. However, YSR states resonantly enhance the Andreev transport [15, 66, 67]. Then, a Cooper pair is transferred into/ out of the condensate via both  $u$  and  $v$  and the state occupation is unchanged (Fig. 7c, right panel). Hence, the many-body ground state is conserved and no relaxation is required for a continuous current. Both transport mechanisms occur with the same bias threshold and it is a priori ambiguous, which of the two is dominating.

Beside single atomic impurities, also quantum dots with odd filling can induce YSR states when they are coupled to at least one superconducting lead. These states can be accessed by transport experiments [68–75]. By means of gate potentials, one can tune the energy of the bound state and drive the singlet-doublet phase transition of the quantum ground state [68].

These transport measurements are typically interpreted in terms of Andreev processes due to the strong tunneling coupling strength and are referred to as Andreev bound states [68, 70, 71, 73]. On the contrary,  $dI/dV$  spectra in scanning tunneling experiments are usually directly linked to the weight of  $u$  and  $v$  of the YSR wave function [28, 49]. However, this assumption holds only for single-particle tunneling. In order to shed light on the different contributions to tunneling, in Ref. [47], the excitation spectrum on Mn adatoms on Pb(111) was probed as a function of junction resistance.

In Figure 7a a change in the relative weight of resonances  $+\alpha$  and  $-\alpha$  is observed when measuring the  $dI/dV$  with a superconducting Pb tip at different tip-sample distances, *i.e.*, with decreasing junction resistance from top to bottom. Figure 7b presents a quantitative analysis over five orders of magnitude of normal state junction resistance of this YSR excitation and its thermal counterpart ( $\pm\beta$ ). At large tip-sample distances (low conductance), a linear increase of all intensities is observed over several orders of magnitude of normal state conductance. At higher conductance, a sublinear behavior is detected and a crossover of the intensities of the electron- and hole-like part is observed for both, the YSR resonances ( $\pm\alpha$ ) and their thermal counterparts ( $\pm\beta$ ).

Qualitatively, this is understood considering the transport as sketched in Fig. 7c. A single-particle current at positive bias is proportional to the product of the relaxation rate  $\Gamma_1$  and the tunneling rate  $\Gamma_e$ , which in turn scales with the square of  $v$ , the weight of the hole-like component [47]. It is independent of  $u$ , the electron-like component. Consequently, the intensities in  $dI/dV$  spectra at negative and positive bias voltage [ $eV = \pm(\Delta_{\text{tip}} + \epsilon)$ ] reflect the relative weight of  $u$  and  $v$ , respectively. As long as  $\Gamma_e$  is small compared to  $\Gamma_1$ , the single particle current increases linearly with the normal state conductance. When the tunneling rate  $\Gamma_e$  becomes similar or larger than the relaxation rate  $\Gamma_1$ , then the relaxation is limiting the single particle current and yields a sublinear increase compared to the normal state conductance.

Andreev tunneling, on the contrary, proceeds via both,  $u$  and  $v$ . The tunneling rate is then the convolution of  $\Gamma_e$  and  $\Gamma_h$ . It is independent of the relaxation rate  $\Gamma_1$ . Therefore, this process becomes important for strong tunneling couplings, *i.e.*, for large currents. Measured with a superconducting tip, the relative intensity of the hole- and electron-like resonances invert in the spectra at large tunnel coupling. It is noteworthy that, with a metallic tip, Andreev transport yields the same intensities for both resonances, *i.e.*, at positive and negative bias [15], while single-particle tunneling again reflects the asymmetry of the  $u$  and  $v$  component in the wave function [47].

A standard Keldysh calculation of the tunneling current, which used all tunneling rates as well as phenomenological relaxation rates of the excited state ( $\Gamma_1$  and  $\Gamma_2$ ), yielded the fits to the conductance evolution shown in Fig. 7b. The arrows indicate the crossover between single-particle and Andreev-dominated transport. From the fits, the relaxation rates were determined to be in the order of hundreds of picoseconds at 1.2 K. However, it was found that they decreased to  $\approx 6$  ps at a temperature to 4.8 K, which indicates a temperature-driven relaxation process. The analysis, which was based on a single step relaxation as sketched in Fig. 7c, overestimates the temperature-dependence by orders of magni-

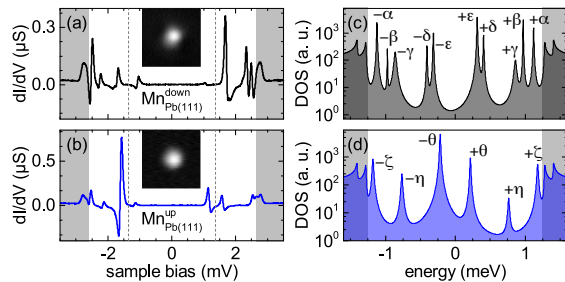


Figure 8. Mn atoms in two different stable adsorption sites on Pb(111). (a,b)  $dI/dV$  spectra of the different Mn adatoms, labeled  $\text{Mn}^{\text{up}}$  and  $\text{Mn}^{\text{down}}$  according to their topographic appearance. The shaded areas indicate the two BCS coherence peaks and excitation continuum, the dashed lines the tip gap ( $\pm 1.38$  mV). The insets show topographies of the adatoms. (c) Deconvolved sample DoS the spectrum in (a), which exhibits five YSR resonances. (d) Deconvolved DoS of the spectrum in (b). There are three YSR resonances. Figure adapted from Ref. [53].

tude. This points towards a relaxation cascade involving more than one YSR resonance of the excitation spectrum.

The measurements show that tunneling experiments can be used to extract quantitative information on the electron and hole component of the YSR states, as well as on the relaxation rates.

#### IV. ORBITAL CHARACTER OF YU-SHIBA-RUSINOV STATES

In Section III, we discussed the transport mechanism through YSR resonances within the superconducting gap disregarding the number of YSR resonances. In literature, several experiments were described, in which more than one pair of subgap resonances had been observed [29, 30, 47, 52, 61]. It was suggested that the coupling to other degrees of freedom, like magnetocrystalline anisotropy [10], or vibrations [11] can explain the experimental observation of several YSR states [52]. Before including possible additional excitations in the discussion (see Section V C below), we point out that a single impurity can bear multiple YSR states due to the presence of several resonant scattering channels.

Early experiments [29, 30] linked multiple resonant YSR states to scattering channels with different angular momenta ( $l = 0, 1, 2, \dots$ ) [44, 45]. Only in 2008, Moca and coworkers showed theoretically that, beside several scattering channels, the internal, *i.e.*, orbital structure of the impurity plays a decisive role in the number and nature of YSR states in the excitation spectrum [9]. Transition metal atoms carry their spin in form of unpaired electrons in the  $d$  shell. The local environment, *i.e.*, the crystal field experienced by the impurity (partially) lifts the degeneracy of the  $d$  levels depending on their orientation. This in turn yields an orbital-dependent potential

and exchange coupling with the substrate, which is imprinted in the YSR states.

For example, Mn adatoms on Pb are expected to be in a +2 oxidation state and host an unpaired electron in each of the five  $d$  levels. Because of the  $S$ -state nature of the ion, only conduction electrons with  $l = 2$  are scattered [76]. This results in five YSR states, some of which can still be degenerate because of the actual symmetry of the environment.

Mn adatoms on Pb(111) acquire two stable adsorption sites which differ in apparent height by  $\approx 0.6$  Å (Fig. 8) [53]. For the higher species with a symmetric appearance three pairs of YSR resonances are observed (Fig. 8b,d). This is in line with a threefold symmetric hollow adsorption site on the (111) lattice, which splits the  $d$  levels into three subsets, the two-fold degenerate  $d_{xz,yz}$  and  $d_{xy,x^2-y^2}$ , and the non-degenerate  $d_{z^2}$ . Each of these subsets is at the origin of one of the pairs of YSR states. Yet, for the second stable adsorption site for adatoms on the (111) surface with an asymmetric topographic appearance and a lower apparent height (Fig. 8a,c),  $dI/dV$  spectra exhibit five pairs of YSR resonances, which implies a complete lifting of all  $d$  level degeneracies caused by the absence of higher spatial symmetry [53]. Similarly, also for Cr adatoms on Pb(111), five YSR states are observed (see below) [54].

In order to unambiguously link a single pair of YSR states to a certain  $d$  level, a symmetry match of the adsorption site and the  $d$  levels is favorable. A hollow-site adsorption on a fourfold-symmetric Pb(001) surface yields a square pyramidal coordination, matching the symmetries of the  $d$  levels. This coordination geometry lifts all degeneracies except the degeneracy of the  $d_{xz}$  and  $d_{yz}$ . Yet, the  $d_{xy}$  orbital is close in energy to (or even degenerate with) these  $d_{\pi}$  orbitals. The energy difference depends on the in-plane and out-of-plane nearest-neighbor distance.

Mn adatoms on Pb(001) (Fig. 9a,b) induce a pair of dominating resonances  $\pm\beta$  and two faint pairs of resonances ( $\pm\alpha$  and  $\pm\gamma$ ) [53]. This is in line with the above described coordination geometry assuming (almost) degenerate  $d_{xy}$  and  $d_{xz,yz}$ . Figure 9c presents  $dI/dV$  maps at the energy of the three bound states, which reveal a characteristic spatial pattern.  $\pm\beta$  are most intense and mainly circular symmetric (note the stretched color code of the  $dI/dV$  maps). These YSR resonances originate from the  $d_{z^2}$  orbital because this orbital has a  $C_1$  symmetry and the strongest wave function overlap with the tip. The maps of  $\pm\alpha$  and  $\pm\gamma$  all exhibit fourfold symmetric patterns, which match the symmetries of the remaining  $d$  levels. While  $\pm\gamma$  is linked to the degenerate  $d_{xz,yz}$  and  $d_{xy}$  orbitals as can be inferred from a splitting of these resonances in the presence of variations in the local environment, the  $d_{x^2-y^2}$  orbital is at the origin of resonances  $\pm\alpha$  [53].

The studies performed on Mn/Pb(111) revealed the

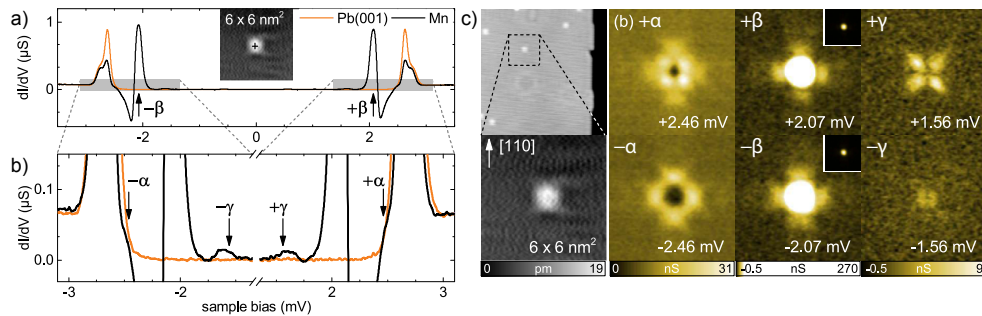


Figure 9. Mn adatoms on Pb(001). a) and b) The  $dI/dV$  spectrum above the adatom unveils three pairs of YSR resonances. c) Topography (left) and  $dI/dV$  maps at the energies of the YSR resonances  $\pm\alpha$ ,  $\pm\beta$ , and  $\pm\gamma$ . The maps reveal the fourfold symmetry of the  $d$  levels and the surface. Figure adapted from Ref. [53].

existence of two atomic configurations, each with a different YSR fingerprint. A similar experimental study on the Cr/Pb(111) system was supported by Density Functional Simulations [54] which unveiled that a subsurface configuration with the impurity atom embedded underneath the top-most Pb layer was energetically preferred (Fig. 10a). Density Functional Theory (DFT) calculations determined that the barrier for Cr atoms to reach the subsurface site through hollow sites of the (111) surface is only 21 meV, which is smaller than the lateral diffusion barriers and can easily be overcome by "hot" adatoms before thermalisation. Subsurface Cr impurities show spectra full of intra-gap features attributed to five YSR excitations (Fig. 10c). With support of DFT calculations, these were interpreted as originating from the five half-filled  $d$  orbitals of Cr, which act as spin-polarized scattering channels. Similar to the case of Mn atoms of lower apparent height ( $\text{Mn}^{\text{down}}$ ), the local symmetry is reduced leading to a breaking of all degeneracies of the  $d$ -derived resonances and, consequently, to YSR states of different coupling strength and, hence, energy.

Although the DFT calculations reveal that the Cr states are strongly mixed with Pb bands, the five spin-polarized channels maintain some degree of the atomic  $d$  character (Fig. 10b). Hence, in a first approximation, they can be treated as five independent channels with a different exchange interaction  $J_n$ . We can use the computed single-particle wave function of the five scattering channels for a calculation of the Bogoliubov quasiparticle coefficients  $|u_\mu(\mathbf{r})|^2$  and  $|v_\mu(\mathbf{r})|^2$ . These represent the local DoS of the particle and hole components, respectively. The spatial maps of these amplitudes (Fig. 10d) show that, while the  $|u_\mu(\mathbf{r})|^2$  component resemble closely the shape of the scattering orbital, the corresponding hole component differs strongly. Such particle-hole asymmetry in the shape of Shiba components was also observed in the experimental maps (Fig. 10c) of the YSR excitations. As expected the simulated orbital shapes can be recognized in some of the particle YSR maps (sample bias  $> 0$ ), while the corresponding hole maps clearly deviate.

Interestingly, one of the YSR states ( $\epsilon_4$ ) shows a particle-hole reversal in the spatial pattern of its YSR excitations: the calculated  $|u_\mu(\mathbf{r})|^2$  component matches the experimental map at negative bias. This reversal is an indication of this channel undergoing a transition to a new correlated ground state (as described in Fig. 2). As first pointed out by Sakurai [41], a critical point occurs for sufficiently large values of  $J_n\rho_s$ , such that the YSR excitation energy becomes zero. This results in the new ground state of the many-body state (see Fig. 2). In this situation, the magnetic impurity becomes locally screened, as pictorially described in Fig. 3. Indeed, for the Cr/Pb(111) system, DFT simulations [54] showed that the alignment of the YSR excitations in the gap is very sensitive to the degree of hybridization  $\Gamma_n$ , the Coulomb constant  $U_n$ , and the energy of the spin-polarized state. It is thus possible that a fraction of scattering channels undergoes the transition to a screened singlet state, while others remain in the double ground state.

## V. QUANTUM-PHASE TRANSITION FROM A KONDO-CORRELATED TO A SUPERCONDUCTING GROUND STATE

In Section IV we reported how the reduced symmetry around the magnetic atom results in a lifting of the orbital degeneracy and an orbital-dependent exchange potential  $J_n$ , which bears multiple bound states in the gap. In realistic systems, the exchange scattering potential  $J_n$  also leads to quantum fluctuations of the impurity spin due to scattering with conduction band electrons, bearing the Kondo effect. For a normal metal, Kondo scattering results in screening of the impurity magnetic moment and the formation of a singlet ground state. As discussed in Section II A, the formation of the superconducting singlet state competes with the Kondo singlet formation. The result is the coexistence of Kondo screening with the formation of YSR states. Changes in the relative strength of the superconducting pairing and the exchange scattering

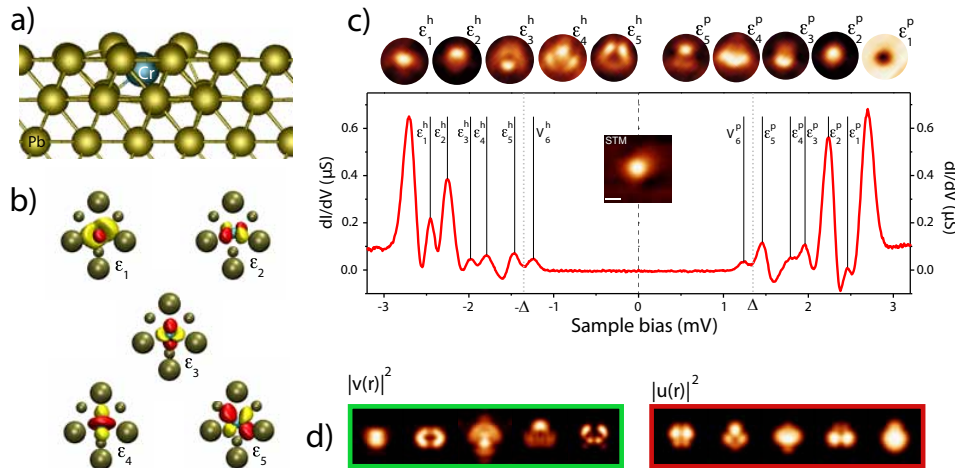


Figure 10. Cr atoms on Pb(111): (a) Results of a full DFT relaxation showing the most stable position of a Cr atom (blue) embedded under the surface of Pb(111). (b) Top-view of wave function amplitude isosurfaces for the five spin-polarized orbitals of embedded Cr, including in yellow, the seven closest Pb atoms. These five states are the only ones originating from the original  $d$ -manifold of the Cr atom with relevant weight. (c)  $dI/dV$  spectrum on a Cr atom. The five peaks labeled  $\epsilon_n^{(h,p)}$  represent the particle (p) and hole (h) excitations of the five YSR states. The peaks labeled  $\nu_5^{(h,p)}$  are the thermal replica of  $\epsilon_5^{(h,p)}$ . The maps on top of the graph depict the amplitude of the peaks in a region of about 2 nm diameter around the impurity. (d) Simulation of particle and hole components of the Bogoliubov quasiparticles for each scattering channel shown in (b). Figure adapted from Ref. [54].

can drive the system through a quantum phase transition separating the two different magnetic ground states.

Ideal systems to study the increasing role of Kondo screening in a superconductor with exchange scattering are hybrid superconductor-quantum dot three-terminal devices. Here, the YSR physics is represented by Andreev bound states at the superconductor-quantum dot interface and the strength of their coupling to the superconductor can be continuously tuned by external gating fields.

#### A. Multiple magnetic ground states in a magnetic molecular system

Another approach to trace the quantum phase transition was realised by taking advantage of a multitude of different adsorption sites of magnetic metal-organic molecules on top of a superconducting surface. Similar to atomic impurities, magnetic molecules such as transition metal phthalocyanines (Pc) on superconductor surfaces also show YSR excitations [49, 52, 60]. The magnetism originates from the incomplete  $d$  shell of the metal ion and its exchange coupling with substrate electrons and Cooper pairs. The (organic) ligand field around the metal ion causes a finite spin anisotropy in these systems, favouring a certain spin orientation over others, and, hence, yields a characteristic excitation multiplet.

A transition between two different ground states

was observed by studying excitation spectra of MnPc molecules on Pb(111). MnPc molecules arrange in square molecular islands (Fig. 11a), where each molecule lies over a distinct atomic site, showing YSR peaks at different energy positions depending on this site. The differences have been ascribed to small variations in the adsorption site, which crucially affect the strength of the exchange scattering. The result is a peculiar Moiré pattern of interaction strength, which can be *visualized* in constant-height current images at tunneling bias voltages inside the superconducting gap (Fig. 11b).

The diversity of possible sites of MnPc on Pb(111) allows us to explore a continuous range of exchange interaction strengths  $J$  in a single experiment simply by selecting different positions in the layer. Figure 11 shows a stack of spectra of 137 different molecules ordered according to the position of the largest YSR spectral peak. We find a broad range of peak alignments, simulating an experiment with a tunable exchange interaction. If we assume that the largest peak corresponds to the  $u(r)$  component, a larger negative bias voltage denotes a larger exchange constant  $J$ . In this case, the plot is ordered from stronger to weaker  $J$ , from top to bottom. At  $\pm\Delta$ , the stack plot also shows the crossings of the YSR resonances corresponding to the  $u$  component with the thermal replica of the  $v$  component and vice versa. This crossing corresponds to the critical point mentioned above, where YSR excitations reach zero energy and separate two different quantum ground states

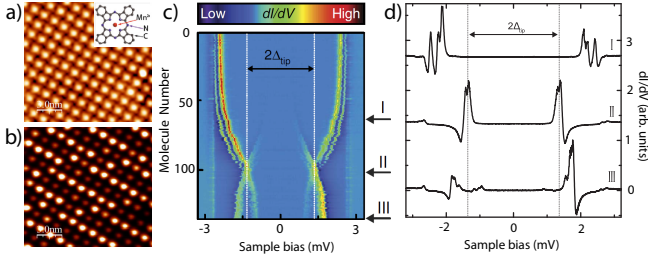


Figure 11. MnPc on Pb(111): (a) Constant current STM image and (b) the corresponding constant-height current map inside the superconducting gap ( $V = 1.2$  meV) of an island of MnPc on Pb(111). The current map shows that each molecule has a different "brightness" (*i.e.*, transmission) depending on the alignment of YSR states with respect to the coherence peaks of the superconducting tip. (c) Colour plot of stacked  $dI/dV$  spectra of 137 MnPc molecules. The spectra are ordered from top to bottom following the energy position of the most intense YSR peak. The two ground states are indicated with arrows, as region I (Kondo ground state) and region III (free spin ground state). Region II corresponds to the crossing point between the two ground state's. (d) Three selected  $dI/dV$  spectra extracted from the stacked plot, one at each region of (c). Both positive and negative energy YSR excitations appear split into three peaks. As discussed in section 5.3, this multiplet is due to the effect of molecular anisotropy in the YSR states. Figure adapted from Ref. [49] (panel a and b) and Ref. [52] (panels c and d).

(Fig. 2). Above the critical point (region I), the larger interaction strength leads to a screened ground state, *i.e.*, a singlet (see Fig. 3), and the YSR peaks denote a doublet (single-particle) excitation. Below, the ground state correspond to a free-like impurity spin (doublet).

### B. Interplay of Kondo correlations with Yu-Shiba-Rusinov excitations

As mentioned above, Kondo correlations participate in the screening of an impurity spin on a superconductor, and their relevance in the ground state of a quantum spin depends on the strength of the exchange scattering. In the regime where the Kondo energy scale ( $k_B T_K$ ) competes with the pairing energy ( $\Delta$ ), a cross over between two different quantum ground states was predicted by Matsuura [37]. To probe the fundamental relationship between the YSR energy  $\epsilon$  and  $k_B T_K$ , both energy scales have to be determined simultaneously.

For the case of MnPc,  $dI/dV$  plots measured above the critical temperature ( $T_c$ ) of Pb(111) show a characteristic zero-bias resonance attributed to the Kondo effect (Fig. 12b). The linewidth again depends on the molecule investigated. A second (broader) resonance (fitted by a blue dashed line in the plot), which was originally interpreted as an additional Kondo channel, has been recently attributed to a Mn  $d$  state [77]. Com-

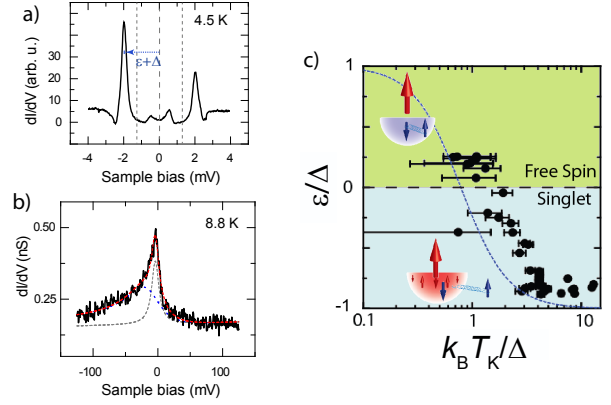


Figure 12. Relation between YSR and Kondo energy scales for MnPc molecules:  $dI/dV$  spectra on a MnPc molecule measured (a) at 4.5 K (below  $T_c$ ) and (b) 8.8 K (above  $T_c$ ), comparing their YSR features with Kondo correlations. In (a), the hole YSR excitation is larger, which signals for this system that it is in a singlet ground state. In (b), a zero-bias peak allows us to quantify the strength of Kondo correlations. (c) Correlation between the bound state energy ( $\epsilon$ ) and the Kondo temperature ( $T_k$ ) extracted from plots like in (a) and (b), respectively. Dots are measured data points for a set of MnPc molecules. The dashed line represents the predicted relation by Matsuura [37]. Figure adapted from Ref. [49].

parison of spectra on each molecule above and below  $T_c$  (Fig. 12a and 12b) confirmed a correlation between the Kondo temperature and the YSR excitation energy [49]. Figure 12c plots the energy position  $\epsilon$  of the larger YSR peak vs. the Kondo energy scale ( $k_B T_K$ ) extracted from spectra like the ones shown in Fig. 12b. The YSR peak shifts towards more positive values as the Kondo energy scale becomes smaller. This corroborates that both spin-scattering processes depend similarly on the magnitude of exchange scattering  $J$ , and their relative strength approaches closely the relation predicted by Matsuura [37]. The crossing of the YSR peaks through zero occurs for  $T_K \sim \Delta$  and reveals the quantum phase transition. For stronger exchange, the ground state is a Kondo singlet. Beyond the critical point, Kondo correlations cannot screen any longer the spin due to the depletion of states inside the superconducting gap (*i.e.*,  $k_B T_K < \Delta$ ). In this case, the competing pairing correlations in the superconductor dominate and the impurity's ground state transforms into a free-spin (doublet).

### C. Effect of magnetic anisotropy in Yu-Shiba-Rusinov states

The spectra in Fig. 11d show that Shiba resonances in MnPc appear split into three narrow peaks, typically with 50–100  $\mu$ eV full width at half maximum, with different intensity, and separated by up to 400  $\mu$ eV. The split peaks are a result of the intrinsic magnetic anisotropy

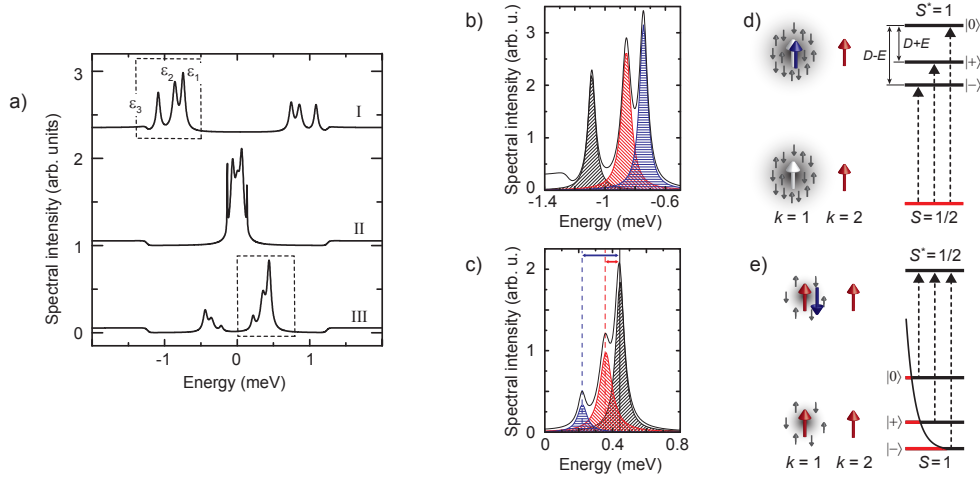


Figure 13. (a) Spectral intensity obtained by deconvolution of the three selected spectra from Fig. 11d. The bound state resonances are labelled  $\epsilon_1$ ,  $\epsilon_2$  and  $\epsilon_3$ , respectively. Dashed boxes highlight the parts in the spectra relevant for the quantitative analysis of the peak areas and splittings. (b) and (c) shows a zoom [marked in (a)] on three peaks for regions I (Kondo screened ground state) and III (free-spin ground state), with the corresponding components extracted as Lorentzian peaks. The area relation between the three peaks in the later case follows close to a Boltzmann-like distribution for the temperature close to the experimental one. (d) and (e) Illustration of the many-body states and the related energy level diagrams. (d) In the Kondo-screened ground state, the spin (white arrow) in scattering channel  $k = 1$  (the dominating channel) is screened, illustrated by grey arrows and shading, and the tunneling electron can enter with its spin (blue arrow) parallel to the spin in  $k = 2$  (the "hidden" scattering channel), increasing the excited state's total spin to  $S^* = 1$ . The excitation scheme including the anisotropy-split excited state is shown by the energy-level diagram with indicated anisotropy parameters  $D$  and  $E$ . (e) In the free-spin ground state, the spin in  $k = 1$  (red arrow) is only partially screened. The tunneling electron enters this state in an anti-parallel alignment, obeying the Pauli exclusion principle and decreasing the spin in the excited state to  $S^* = 1/2$ . Figure adapted from Ref. [52].

of the MnPc molecule, as predicted by Zitko [10], and demonstrated in Ref. [52]. When the magnetic impurity has a spin larger than  $1/2$ , intra-impurity magnetic anisotropy can split its energy levels into a multiplet of  $S_z$  components. The spin  $3/2$  of free MnPc molecules is partially decreased to  $S=1$  at the Pb(111) surface [78], with two spin-polarized orbitals,  $d_{z^2}$  and  $d_{xy}$ . The exchange interaction with the surface is dominated by the  $d_{z^2}$  orbital, whereas the  $d_{xy}$  state remains "hidden" in the molecular plane. Even though there is only one tunneling and scattering channel (the  $d_{z^2}$  orbital), correlations between the two spin-polarized orbitals split the corresponding YSR state into a multiplet. The energy split of the multiplet reflects the magnetic anisotropy of the impurity spin, but is renormalized by the many-body interactions.

However, the essence behind the fine structure is more complex [52]. As pictured in Fig. 7 in Sec. III, transport in the regime of single particle tunneling involves the formation of a transient many-body state, the YSR excitation, with a different occupation than the ground state. The lifetime of the excited state is, as shown in Sec. III, in the order of hundreds of ps at 1.2 K. This reduces the excitation linewidth such that the measurement becomes sensitive to the magnetic anisotropy of the transient state. Hence, the anisotropy splits the excited state

into different energy levels.

The spectral multiplet thus shall reflect all possible transitions connecting the ground state multiplet to the transient state multiplet maintaining angular momentum conservation. We note that, while the population of the ground state's multiplet should follow a Boltzmann statistics, the excited state's multiplet can be accessed with similar probability. Therefore, the amplitudes of the peaks in the Shiba substructure shall reflect the strength of each possible transition, allowing to determine its origin.

The sequence of spectral peaks in the deconvolved spectra depicted Fig. 13a illustrates the peculiar variation of the spectral intensity of each peak according to the ground state. As outlined in Figs. 13b and 13c, in the Kondo screened case (region I in Fig. 11c) all spectra show peaks with similar intensity, independently of their position. On the contrary, the spectral intensity of the peaks in the free-spin ground state (region III) follows a thermal-like distribution of intensities: hole and particle excitations become stronger with their energy, following a Boltzmann-like distribution of the peak areas [52]. From the arguments above, this signals that they correspond to transitions from a multiplet in the  $S=1$  ground state. This triplet state originates from the intra-atomic magnetic exchange of the scattering channel

( $k = 1$  in Fig. 13e) and the hidden spin ( $k = 2$ ), while the single-particle tunneling via the  $k = 1$  channel leads to a  $S^* = 1/2$  transient state.

On the contrary, the similar intensity of triplet excitations in the Kondo-correlated ground state is a fingerprint of transitions to an excited-state multiplet with a transient spin  $S^* = 1$ . As depicted in Fig. 13d, this is fully consistent with the existence of the "hidden" spin in the  $k = 2$  channel accompanying the screened channel  $k = 1$ . It is remarkable that, due to the long lifetime of the excitations, the YSR transient state is sensitive to the intrinsic magnetic anisotropy of the molecule and split into three levels. It is worth mentioning that, since these results probe properties of the YSR many-body state, the observed split corresponds to the intramolecular anisotropy but renormalized by the exchange scattering interactions.

## VI. LATERAL EXTENSION OF YU-SHIBA-RUSINOV STATES

In section IV, we discussed the shape of the YSR states in the close vicinity of the impurity, which reflects the orbital shape of the scattering potential. Moreover, the YSR states show a longer-ranged intensity, which is determined by several characteristic length scales of the superconductor: On the one hand, the coherence length  $\xi$  plays a role, as expected intuitively for a superconducting material. The decay of the YSR wavefunction scales as  $\exp(-r/\xi)$  (see Eq. 3) with the distance  $r$  from the impurity. On the other hand, scattering at an impurity is governed by fermionic scattering processes, which occur on the length scale of the Fermi wavelength. The physical concept relates to the Friedel-like screening of the impurity site. The YSR wavefunction thus exhibits an oscillation with the Fermi wavelength  $\lambda_F$  and an additional  $1/(k_F r)$  decay for an isotropic 3D superconductor (see Eq. 3). We first discuss the contributions to the decay. Typical type I superconductors possess a coherence length in the order of 100 nm, whereas the Fermi wavelength is only in the order of 1 nm. Hence, the decay at close distance around the impurity will be dominated by the Fermi wavelength and, in particular, by the dimensionality of the superconducting substrate, whereas the coherence length has minor influence. Menard and co-workers showed on the quasi-2D superconductor NbSe<sub>2</sub> that one can indeed observe a long-range extension of YSR states [59]. Sub-surface impurities led to an oscillation pattern of the YSR states with significant amplitude of the wave function up to 7 nm away from the impurity site (see Fig. 14). This was explained by the reduced damping of the wave function in 2D compared to 3D, with  $\psi^\pm$  scaling like  $1/\sqrt{k_F r}$  in 2D.

In contrast, Pb is a 3D superconductor. Hence, one may expect a much faster decay of the wavefunction. Sur-

prisingly, Mn atoms on Pb(111) also showed patterns of YSR states up to 4 nm away from the adsorption site (see Fig. 15). It is, however, interesting to note that the YSR states of Mn on Pb(100) (see Fig. 9) were much shorter ranged (only up to 2 nm). Hence, the surface orientation seems to play an important role. Furthermore, we note that the decay is not spherically symmetric, but "beams" extend along the high symmetry directions of the surface. This holds true for 2D and 3D superconductors and can be ascribed to the anisotropy of the band structure of the substrate [42, 45]. Electrons/holes scattered at an impurity are focused into directions, which originate from flat areas of the Fermi surface [79]. This focusing effect enhances the YSR amplitude for these directions and gives rise to a fall-off, which is slower than expected for an isotropic decay. Hence, we can observe the YSR wavefunction nanometers away from the impurity.

The fermionic properties of the scattering processes are also imprinted in an oscillatory pattern of the YSR states. Hence, the wave function does not only decay with the characteristic  $1/(k_F r)$  dependence, but also oscillates with the Fermi wavelength  $\lambda_F$ . Because STM probes the probability density  $|\Psi|^2$ , the observed oscillation is periodic in  $\lambda_F/2$ . Fig. 15 reveals an oscillation around the Mn adatom on Pb(111) with a period of  $\sim 5.8 \text{ \AA}$ , which thus reflects  $\lambda_F \sim 11.6 \text{ \AA}$ . Pb exhibits a complex Fermi surface with two disjoint sheets with significantly different values of the Fermi wave vector  $k_F$  along the different lattice directions [80]. Importantly, the electron-phonon coupling strength is different on the two sheets and gives rise to two distinct superconducting energy gaps [51, 81]. The observation of a single, well-defined oscillation period evidences that the magnetic impurity is predominantly coupled to the corresponding Fermi sheet. In this case of Mn on Pb(111), it reveals the coupling of the impurity spins to the Fermi sheet with mainly  $p-d$  orbital character instead of to the Fermi sheet with mostly  $s-p$  orbital character. Considering the more local nature of the electrons in the  $p-d$ -like bands, they are affected more strongly by a local impurity than extended bands. More importantly, in Sec. IV we have shown that dominantly  $l = 2$  fermions scatter with the unpaired spins in the  $d$  states of Mn as was early predicted by Schrieffer in the case of Kondo scattering [76]. Hence, the restriction to certain angular momenta for efficient scattering favors the  $p-d$ -like band. At far (and intermediate) distances, the impurity appears as a point-like scatterer, which bears a single wave vector of the wave function.

Interestingly, the scattering pattern of the YSR states obey distinct phase differences between the  $u$  and  $v$  components. The observed phase difference [53] depends on the energy of the YSR state and follows the theoretical prediction of Eq. 4 of a point scatterer.

It is noteworthy that, in the case of Cr atoms on Pb(111) films grown on SiC(0001) [54], no oscillatory

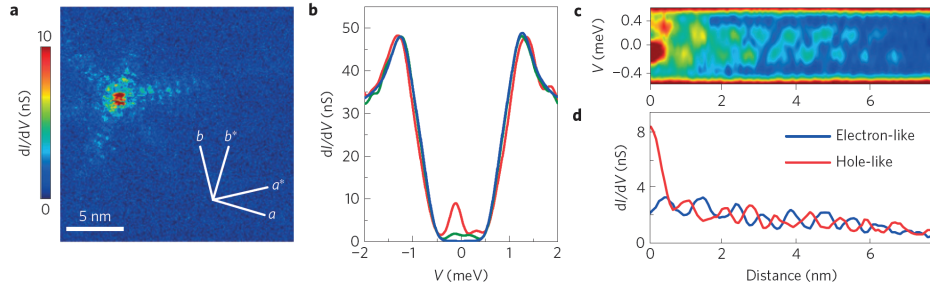


Figure 14. Subsurface impurities in 2H-NbSe<sub>2</sub>. a)  $dI/dV$  map of subsurface impurities in 2H-NbSe<sub>2</sub> show oscillatory falloff of the Shiba wave function. b)  $dI/dV$  spectrum above the center of the scattering pattern. c) pseudo-2D representation of  $dI/dV$  spectra as a function of distance. Oscillatory falloff of the electron- and hole-component of the Shiba wave function. Reprinted by permission from Macmillan Publishers Ltd: Nature Physics [59], copyright 2015.

fall-off was observed. Concurrently, no signs of two-band superconductivity were observed for the Pb films, in contrast to the single-crystal samples [51]. Both findings could be linked to the insufficient films thickness, which does not allow for the  $p-d$ -like band to be fully developed. Hence, there is no preferential scattering with a single band and the focusing effect is absent. Hence, the YSR wave function decays much faster in this case.

## VII. COUPLING OF SHIBA IMPURITIES – FROM DIMERS TO TOPOLOGICAL CHAINS

The extension of the YSR states is a promising avenue for coupling magnetic impurities on a superconductor. Theoretically, the coupling of YSR states has already been discussed since the advent of the understanding of the individual states [33]. The physical picture is based on the spatial overlap of YSR states. The

YSR states thus hybridize, with the hybrid state being described by the linear combination of the YSR states (similar to LCAO theory or to the description of interference patterns due to the overlap of oscillating YSR states [4, 7]). Experimentally, hybrid YSR states have first been seen on dimers of Mn and Cr on Pb(111) [29]. Tunneling spectra revealed a splitting of the YSR states. The corresponding STM images reflected the bonding (anti-bonding) nature of the coupled states via a maximum (zero) intensity at midway between the impurity sites. Recently, a splitting of YSR states has also been observed on dimers of Co-Phthalocyanine molecules adsorbed on the quasi-2D superconductor NbSe<sub>2</sub> [60].

In the limit of dense arrangements of magnetic impurities, the YSR states' overlap may lead to extended bands. These fill and eventually suppress the supercon-

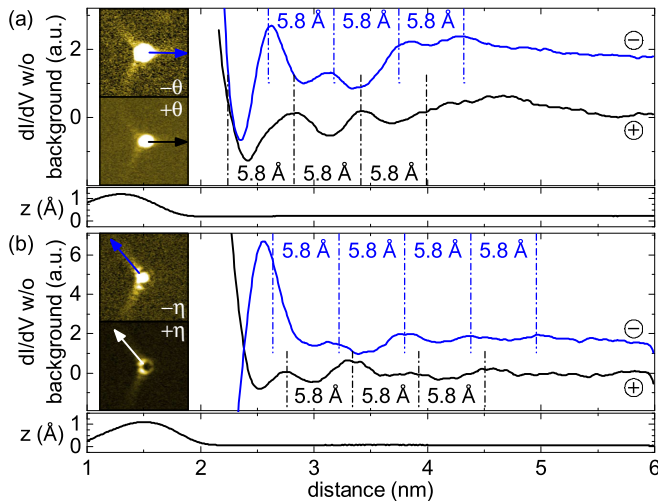


Figure 15. Mn adatoms on Pb(111). Oscillatory modulation of the Shiba wave function for two pairs of bound states ( $\pm\theta$  and  $\pm\eta$ ). Figure adapted from Ref. [53].

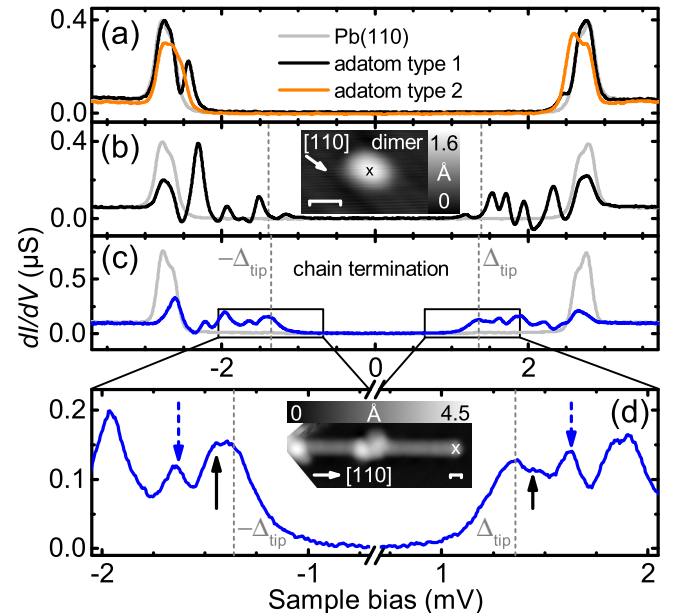


Figure 16. Fe on Pb(111).  $dI/dV$  spectra acquired above two adatom species (a), above an Fe dimer (b), and above the end of an iron chain (c and d). Figure adapted from Ref. [82].

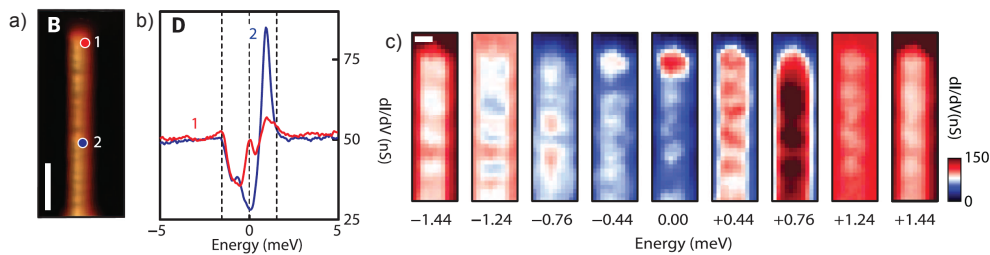


Figure 17. Fe chains on Pb(110). b)  $dI/dV$  spectrum above the center (2) and the end (1) of the iron chain shown in (a). c)  $dI/dV$  maps of the iron chain at different energies around  $E_F$ . The zero energy map shows an intensity localization at the chain end. From Ref. [83]. Reprint with permission from AAAS.

ducting energy gap [30]. An intriguing example for the formation of YSR bands are one-dimensional chains of transition metal adatoms on a superconducting Pb surface. Employing a Pb(110) surface steers the assembly of Fe [82–85] and Co [86] chains along the troughs of the surface. Whereas dimers of Fe atoms in these troughs already show an increase in the number of YSR resonances in the superconducting energy gap (Fig. 16b), the chains show a rich resonance structure. While the dominant resonances can be interpreted as van Hove singularities of YSR bands, the rich and varying structure along the chain results from confinement effects in the finite chain and variations in the local potential [82, 86, 87].

However, the importance of these chains cannot only be ascribed to the fundamental nature of the YSR bands, but also to their potential to host Majorana zero modes at their terminations. These zero energy modes are the condensed matter equivalent to Majorana Fermions [88] in particle physics and possess numerous interesting properties, such as obeying non-Abelian statistics [1–3]. Topological superconductivity is a crucial prerequisite for Majorana zero modes. On an  $s$ -wave superconductor, this can be realized either by helical spin chains [89–91] or by ferromagnetic chains in the presence of strong spin-orbit coupling, as it occurs in Pb [83, 87, 92]. The induced  $p$ -wave superconducting gap protects the topological nature of the band structure. The first putative realization of such a system are the above mentioned Fe chains on Pb(110), where an odd number of spin-polarized band cross the Fermi level. These provide the origin of the Majorana states at the chain ends [83, 92].

The prospect of using Majorana states for topological quantum computing has driven the investigation of the formation of Majorana bound states in proximity coupled chains of transition metal atoms on a superconductor to the forefront of research in solid state physics.

## VIII. CONCLUSIONS AND FUTURE DIRECTIONS

In summary, we described the latest experimental results on individual magnetic adsorbates on  $s$ -wave super-

conductors. In combination with theory, tremendous advances have been made in the fundamental understanding of the origin of multiple subgap excitations and their relation to the many-body quantum states. The investigations also bridged the gap between STM-based research and quantum nanoelectronics. Despite of this progress, new experiments are required to go beyond the current state-of-the-art, in particular in view of the construction of adatom-based nanostructures. One interesting aspect is the coupling between adatoms, which is currently treated by theory in great detail. The coupling mechanism, its length scale, as well as resulting magnetic ground states are modeled [4, 18, 19]. Yet, experimental evidence of the different scenarios is mostly still missing. While these questions are again of fundamental nature, they also form the basis for understanding the coupling in larger adatom structures, eventually leading to one-dimensional and two-dimensional topological structures.

## ACKNOWLEDGMENTS

We are thankful for fruitful discussion with Gelavizh Ahmadi, Laëtizia Farinacci, Nino Hatter, Nicolas Lorente, Felix von Oppen, Yang Peng, Falko Pientka, Gaël Reecht, Dimitri Roditchev, Michael Ruby, Gunnar Schulze, Clemens Winkelmann. We acknowledge financial support by the Deutsche Forschungsgemeinschaft by Grant No. FR2726/4 (K. J. F.) and Grant No. HE7368/2 (B. W. H.), by the European Research Council through Consolidator Grant *NanoSpin* (K. J. F.).

## REFERENCES

- 
- \* bheinrich@physik.fu-berlin.de
  - † ji.pascual@nanogune.eu
  - ‡ franke@physik.fu-berlin.de
- [1] J. Alicea, Rep. Prog. Phys. **75**, 076501 (2012).

- [2] C. W. J. Beenakker, Annual Review of Condensed Matter Physics **4**, 15 (2013).
- [3] S. Elliott and M. Franz, Review of Modern Physics **87**, 34 (2015).
- [4] D. Morr and N. Stavropoulos, Physical Review B **67**, 020502(R) (2003).
- [5] D. K. Morr and R. H. Nyberg, Physical Review B **68**, 60505 (2003).
- [6] A. V. Balatsky, I. Vekhter, and J.-X. Zhu, Reviews of Modern Physics **78**, 373 (2006).
- [7] D. K. Morr and J. Yoon, Physical Review B **73**, 224511 (2006).
- [8] J. Bauer, A. Oguri, and A. C. Hewson, Journal of Physics: Condensed Matter **19**, 486211 (2007).
- [9] C. Moca, E. Demler, B. Jankó, and G. Zaránd, Physical Review B **77**, 174516 (2008).
- [10] R. Zitko, O. Bodensiek, and T. Pruschke, Physical Review B **83**, 054512 (2011).
- [11] D. Golez, J. Bonca, and R. Zitko, Physical Review B **86**, 085142 (2012).
- [12] M. Kharitonov, T. Proslir, A. Glatz, and M. J. Pellin, Physical Review B **86**, 024514 (2012), arXiv:1109.3395.
- [13] N. Y. Yao, L. I. Glazman, E. A. Demler, M. D. Lukin, and J. D. Sau, Physical Review Letters **113**, 087202 (2014).
- [14] N. Y. Yao, C. P. Moca, I. Weymann, J. D. Sau, M. D. Lukin, E. A. Demler, and G. Zaránd, Physical Review B **90**, 241108 (2014).
- [15] I. Martin and D. Mozysky, Physical Review B **90**, 100508 (2014).
- [16] R. Zitko, Physical Review B **91**, 165116 (2015).
- [17] R. Zitko, J. S. Lim, R. López, and R. Aguado, Physical Review B **91**, 045441 (2015).
- [18] T. Meng, J. Klinovaja, S. Hoffman, P. Simon, and D. Loss, Physical Review B **92**, 064503 (2015).
- [19] S. Hoffman, J. Klinovaja, T. Meng, and D. Loss, Physical Review B **92**, 125422 (2015).
- [20] Y. Kim, J. Zhang, E. Rossi, and R. M. Lutchyn, Physical Review Letters **114**, 236804 (2015).
- [21] G. Kirsanskas, M. Goldstein, K. Flensberg, L. I. Glazman, and J. Paaske, Physical Review B - Condensed Matter and Materials Physics **92**, 235422 (2015).
- [22] S. Gopalakrishnan, C. V. Parker, and E. Demler, Physical Review Letters **114**, 045301 (2015).
- [23] S. S. Pershoguba, K. Björnson, A. M. Black-Schaffer, and A. V. Balatsky, Physical Review Letters **115**, 116602 (2015).
- [24] S. S. Pershoguba, S. Nakosai, and A. V. Balatsky, Physical Review B **94**, 064513 (2016).
- [25] R. Zitko, Physical Review B **93**, 195125 (2016).
- [26] V. Kaladzhyan, C. Bena, and P. Simon, Physical Review B **93**, 214514 (2016).
- [27] J. L. Lado and J. Fernandez-Rossier, 2D Materials **3**, 025001 (2016).
- [28] A. Yazdani, B. A. Jones, C. P. Lutz, M. F. Crommie, and D. M. Eigler, Science **275**, 1767 (1997).
- [29] S.-H. Ji, T. Zhang, Y.-S. Fu, X. Chen, X.-C. Ma, J. Li, W.-H. Duan, J.-F. Jia, and Q.-K. Xue, Physical Review Letters **100**, 226801 (2008).
- [30] S.-H. H. Ji, T. Zhang, Y.-S. S. Fu, X. Chen, J.-F. F. Jia, Q.-K. K. Xue, and X.-C. C. Ma, Applied Physics Letters **96**, 073113 (2010).
- [31] L. Yu, Acta Physica Sinica **21**, 75 (1965).
- [32] H. Shiba, Progress of Theoretical Physics **40**, 435 (1968).
- [33] A. I. Rusinov, ZhETF Pisma Redaktsiui **9**, 146 (1968).
- [34] A. I. Rusinov, Soviet Journal of Experimental and Theoretical Physics **29**, 1101 (1969).
- [35] A. A. Abrikosov and L. P. Gor'kov, ZhETF **39**, 1781 (1960).
- [36] J. Kondo, Progress of Theoretical Physics **32**, 37 (1964).
- [37] T. Matsura, Progress of Theoretical Physics **57**, 1823 (1977).
- [38] We restrict our discussion to the most interesting case, *i.e.*, to antiferromagnetic exchange coupling. For the ferromagnetic case, see, *e.g.*, Balatsky *et al.* [6].
- [39] K. Satori, H. Shiba, O. Sakai, and Y. Shimizu, Journal of the Physical Society of Japan **61**, 3239 (1992).
- [40] O. Sakai, Y. Shimizu, H. Shiba, and K. Satori, Journal of the Physical Society of Japan **62**, 3181 (1993).
- [41] A. Sakurai, Progress of Theoretical Physics **44**, 1472 (1970).
- [42] M. I. Salkola, A. V. Balatsky, and J. R. Schrieffer, Physical Review B **55**, 12648 (1997).
- [43] J. Bauer, J. I. Pascual, and K. J. Franke, Physical Review B **87**, 075125 (2013).
- [44] M. Flatté and J. Byers, Physical Review Letters **78**, 3761 (1997).
- [45] M. E. Flatté and J. M. Byers, Physical Review B **56**, 11213 (1997).
- [46] J. Zittartz and E. Müller-Hartmann, Zeitschrift für Physik **232**, 11 (1970).
- [47] M. Ruby, F. Pientka, Y. Peng, F. von Oppen, B. W. Heinrich, and K. J. Franke, Physical Review Letters **115**, 087001 (2015).
- [48] M. Ternes, W.-D. Schneider, J.-C. Cuevas, C. P. Lutz, C. F. Hirjibehedin, and A. J. Heinrich, Phys. Rev. B **74**, 132501 (2006).
- [49] K. J. Franke, G. Schulze, and J. I. Pascual, Science **332**, 940 (2011).
- [50] B. W. Heinrich, L. Braun, J. I. Pascual, and K. J. Franke, Nature Physics **9**, 765 (2013).
- [51] M. Ruby, B. W. Heinrich, J. I. Pascual, and K. J. Franke, Physical Review Letters **114**, 157001 (2015).
- [52] N. Hatter, B. W. Heinrich, M. Ruby, J. I. Pascual, and K. J. Franke, Nature Communications **6**, 8988 (2015).
- [53] M. Ruby, Y. Peng, F. von Oppen, B. W. Heinrich, and K. J. Franke, Physical Review Letters **117**, 186801 (2016).
- [54] D.-J. Choi, C. Rubio-Verdú, J. de Bruijckere, M. M. Ugeda, N. Lorente, and J. I. Pascual, Nat. Comm. **8**, 15175 (2017).
- [55] V. Madhavan, W. Chen, T. Jamneala, M. F. Crommie, and N. S. Wingreen, Science **280**, 567 (1998).
- [56] J. Li, W.-D. Schneider, R. Berndt, and B. Delley, Phys. Rev. Lett. **80**, 2893 (1998).
- [57] A. J. Heinrich, J. A. Gupta, C. P. Lutz, and D. M. Eigler, Science (New York, N.Y.) **306**, 466 (2004).
- [58] Y. Yayon, V. W. Brar, L. Senapati, S. C. Erwin, and M. F. Crommie, Phys. Rev. Lett. **99**, 067202 (2007).
- [59] G. C. Ménard, S. Guisart, C. Brun, S. Pons, V. S. Stolyarov, F. Debontridder, M. V. Leclerc, E. Janod, L. Cario, D. Roditchev, P. Simon, and T. Cren, Nature Physics **11**, 1013 (2015).
- [60] S. Kezilebieke, M. Dvorak, T. Ojanen, and P. Liljeroth, arXiv:1701.03288.
- [61] M. T. Randeria, B. E. Feldman, I. K. Drozdov, and A. Yazdani, Physical Review B **93**, 161115(R) (2016).

- [62] E. W. Hudson, S. H. Pan, A. K. Gupta, K.-W. Ng, and J. C. Davis, *Science* **285**, 88 (1999).
- [63] A. Yazdani, C. Howald, C. Lutz, a. Kapitulnik, and D. Eigler, *Physical Review Letters* **83**, 176 (1999).
- [64] S. Pan, E. Hudson, K. Lang, H. Eisaki, S. Uchida, and J. Davis, *Nature* **403**, 746 (2000).
- [65] E. W. Hudson, K. M. Lang, V. Madhavan, S. H. Pan, H. Eisaki, and J. C. Davis, *Nature* **411**, 920 (2001).
- [66] B. M. Andersen, K. Flensberg, V. Koerting, and J. Paaske, *Physical Review Letters* **107**, 256802 (2011).
- [67] P. A. Ioselevich and M. V. Feigel'Man, *New Journal of Physics* **15**, 055011 (2013).
- [68] R. S. Deacon, Y. Tanaka, A. Oiwa, R. Sakano, K. Yoshida, K. Shibata, K. Hirakawa, and S. Tarucha, *Physical Review Letters* **104**, 076805 (2010).
- [69] S. De Franceschi, L. Kouwenhoven, C. Schönberger, and W. Wernsdorfer, *Nature Nanotechnology* **5**, 703 (2010).
- [70] J.-D. Pillet, C. H. L. Quay, P. Morfin, C. Bena, A. L. Yeyati, and P. Joyez, *Nature Physics* **6**, 965 (2010).
- [71] T. Dirks, T. L. Hughes, S. Lal, B. Uchoa, Y.-F. Chen, C. Chialvo, P. M. Goldbart, and N. Mason, *Nature Physics* **7**, 386 (2010).
- [72] W. Chang, V. E. Manucharyan, T. S. Jespersen, J. Nygård, and C. M. Marcus, *Physical Review Letters* **110**, 217005 (2013).
- [73] E. J. H. Lee, X. Jiang, M. Houzet, R. Aguado, C. M. Lieber, and S. De Franceschi, *Nature Nanotechnology* **9**, 79 (2014).
- [74] D. M. T. V. Zanten, F. Balestro, H. Courtois, and C. B. Winkelmann, *Phys. Rev. B* **92**, 184501 (2015).
- [75] A. Jellinggaard, K. Grove-Rasmussen, M. H. Madsen, and J. Nygård, *Physical Review B* **94**, 064520 (2016).
- [76] J. R. Schrieffer, *Journal of Applied Physics* **38**, 1143 (1967).
- [77] J. Kügel, M. Karolak, A. Krönlein, J. Senkpiel, P.-J. Hsu, G. Sangiovanni, and M. Bode, *Physical Review B* **91**, 235130 (2015).
- [78] D. Jacob, M. Soriano, and J. J. Palacios, *Physical Review B* **88**, 134417 (2013).
- [79] A. Weismann, M. Wenderoth, S. Lounis, P. Zahn, N. Quaas, R. G. Ulbrich, P. H. Dederichs, and S. Blügel, *Science* **323**, 1190 (2009).
- [80] G. I. Lykken, A. L. Geiger, K. S. Dy, and E. Mitchell, *Physical Review B* **4**, 1523 (1971).
- [81] A. Floris, A. Sanna, S. Massidda, and E. K. U. Gross, *Phys. Rev. B* **75**, 54508 (2007).
- [82] M. Ruby, F. Pientka, Y. Peng, F. von Oppen, B. W. Heinrich, and K. J. Franke, *Physical Review Letters* **115**, 197204 (2015).
- [83] S. Nadj-Perge, I. K. Drozdov, J. Li, H. Chen, S. Jeon, J. Seo, A. H. MacDonald, B. A. Bernevig, and A. Yazdani, *Science* **346**, 602 (2014).
- [84] R. Pawlak, M. Kisiel, J. Klinovaja, T. Meier, S. Kawai, T. Glatzel, D. Loss, and E. Meyer, *npj Quantum Information* **2**, 16035 (2016).
- [85] B. E. Feldman, M. T. Randeria, J. Li, S. Jeon, Y. Xie, Z. Wang, I. K. Drozdov, B. A. Bernevig, and A. Yazdani, *Nature Physics* **13**, 286 (2017).
- [86] M. Ruby, B. W. Heinrich, Y. Peng, F. von Oppen, and K. J. Franke, arXiv:1704.05756v1.
- [87] Y. Peng, F. Pientka, and L. I. Glazman, *Phys. Rev. Lett.* **114**, 106801 (2015).
- [88] E. Majorana, *Nuovo Cimento* **14**, 171 (1937).
- [89] S. Nadj-Perge, I. K. Drozdov, B. A. Bernevig, and A. Yazdani, *Phys. Rev. B* **88**, 020407(R) (2013).
- [90] F. Pientka, L. I. Glazman, and F. V. Oppen, *Phys. Rev. B* **88**, 155420 (2013).
- [91] J. Klinovaja, P. Stano, A. Yazdani, and D. Loss, *Phys. Rev. Lett.* **111**, 186805 (2013).
- [92] J. Li, H. Chen, I. K. Drozdov, A. Yazdani, B. A. Bernevig, and A. H. MacDonald, *Physical Review B* **90**, 235433 (2014).